National Research University
«Higher School of Economics»

as a manuscript

Afanasev Anton

Algorithms for multipoint measurements processing in distributed space systems

Ph. D. Thesis summary

for the purpose of obtaining academic degree
Doctor of Philosophy in Engineering

Academic supervisor:
Ph. D., associate professor
Anton B. Ivanov

Moscow, 2023

General Description of the Work

The relevance of research

The thesis explores the relevance and importance of distributed space systems, which utilize multi-spacecraft formations to replace large single-satellite architectures. These systems aim to enhance mission reliability, achievable outcomes, and cost-effectiveness. While single-satellite missions offer advantages in terms of precision and functionality, distributed architectures provide improved flexibility and adaptability to accommodate structural and functional changes.

Distributed measurements play a crucial role in these systems, offering a multitude of benefits. Firstly, they enable improved data accuracy by collecting measurements from multiple points in space, mitigating individual measurement errors and providing more reliable observations. Secondly, distributed measurements enhance spatial coverage, allowing for comprehensive analysis of phenomena occurring over larger areas of interest. This broader spatial perspective leads to a better understanding of spatial variations and patterns.

Furthermore, distributed measurements offer higher temporal resolution, facilitating the study of dynamic processes, rapid changes, and time-dependent phenomena. By continuously monitoring and collecting data from multiple spacecraft simultaneously, researchers can capture intricate details that would be challenging with single-point measurements alone.

Additionally, distributed systems provide redundancy and fault tolerance. In the event of a failure or malfunction of one spacecraft within a formation, the remaining satellites can continue to operate and provide valuable data. This redundancy increases the reliability and robustness of the measurements, ensuring that critical information is not lost due to single-point failures.

The applications of distributed measurements are versatile and far-reaching. They are instrumental in remote sensing, climate monitoring, space weather analysis, atmospheric studies, Earth observation, and planetary exploration. Leveraging

distributed measurements opens up new avenues for scientific research and advancements in our understanding of the universe. One of the principal issues addressed in the thesis is the collective processing and utilization of data in a swarm of CubeSats, with particular emphasis on the spacecraft's attitude determination and control subsystem. The study illustrates how the swarm can effectively retrieve the actual magnetic field in regions where the swarm satellites are present by processing the exchanged measurement data facilitated through intersatellite links.

The thesis underscores the importance of multipoint measurements processing by a cluster of CubeSats for various space applications. These applications encompass synthetic aperture radars (SAR), optical interferometry, on-orbit inspection and servicing of other spacecraft, and the measurement of spatial gradients in environmental data.

In summary, distributed measurements in space offer improved data accuracy, enhanced spatial coverage, higher temporal resolution, and fault tolerance. They enable comprehensive observations, provide valuable insights into complex phenomena, and contribute to scientific knowledge, technological development, and decision-making processes in space exploration and Earth's environment.

Goal of the research

A goal of the research is to develop a set of algorithms to enhance measurements of environmental phenomena and improve their estimates, using a distributed group of satellites, taking advantage of the multipoint measurements processing and its inference on a variety of space applications.

Objectives of the research

To achieve this goal, the following objectives had to be completed:

1. To research an ability to improve measurements of the geomagnetic field with Kriging interpolation in a swarm of 4 CubeSats.

2. To research on how the ADCS of each CubeSat from a formation of 4 bodies, constituted with magnetometers and sun sensors, can be improved with

measurements exchange and formation structure variation.

3. To research the most effective formations of satellites to make space-based optical observation for on-request short-arc orbit determination of smaller (1 to 10 cm in size) space debris objects in highly-polluted sun-synchronous orbits.

Scientific novelty

1. The Kriging interpolation is proposed for the first time to use as a technique for space-based multipoint measurements processing, increasing accuracy of measured and dependent parameters estimations.

   The powered exponential model function was proposed as the best fit for an empirical semivariogram of geomagnetic field.

   It is suggested to use a measurement history to enhance the accuracy of interpolation.

2. Law of motion for tetrahedral satellites formation is researched for near-circular orbits and the best possible structure was found to perform multipoint measurements with Kriging interpolation.

3. The best configuration of satellites was discovered for a short-arc space debris orbit determination with optical sensors and up to 4 spacecraft.

The highlights of the thesis are:

1. The Kriging interpolation model is suggested to enhance the accuracy of estimation of geomagnetic field, which compares favorable to other interpolators, like inverse distance weighing and splines, since it tales into account variational properties of the considered region.

   The best fit of powered exponential model function is found for an empirical semivariogram of the geomagnetic field.

The Kriging solution for interpolation of geomagnetic field is proven to be robust to the presence of strong model noise, making it possible to use theoretically found semivariograms in real-life missions.

Mean-squared errors of measurements and Kriging interpolation estimates are compared and the latter is found to be more effective, especially for satellite formations with low characteristic size.

Measurements history were used to increase the number of interpolation points, thus increasing the accuracy of geomagnetic field estimation.

2. Mean-squared errors of attitude determination with Extended Kalman Filter and Lyapunov-based controller on magnetometers were compared for scenarios with singular CubeSat and with a swarm of 4 CubeSats, performing measurements exchange and Kriging interpolation. The latter is found to be more effective.

   The rigid body structure with measurements extrapolation and relative motion on a near-circular orbits were used to simulate the work of ADCS for a swarm of 4 CubeSats.

   The tetrahedral formation with relative motion on a near-polar circular orbit was implemented to simulate an ionospheric mission. The relative motion was based on a Hill-Clohessy-Wiltshire equations, maintain the best possible tetrahedron quality and preserve distances between satellites as long as possible. Laws of motion for such formation were derived.

3. Space-based optical observations of small debris to determine their orbit were conducted on a train, general circular orbit and tetrahedron satellites configurations with various number of satellites and various triangulation bases on a sun-synchronous orbits.

   The Extended Information filter was used to produce estimates of radius-vector and linear velocity of a debris, based on measurements of elevation and

azimuth angles. Information filter was chosen instead of Kalman filter due to small processing time of short-arc orbit determination.

All configurations were compared in terms of mean-squared errors of state-space vector estimation, and the best one was recommended to be used in real-life missions.

Practical significance

Results of the work can be used in real-life space missions to increase the accuracy of any sorts of measurements, such as ionospheric missions, distributed SAR missions, debris short-arc orbit determination. Also, the formation of 4 satellites can be used as a generator of accurate geomagnetic field measurements and broadcast the data to neighbouring spacecraft with noisy magnetometers.

Practical significance is confirmed by a participation in a grant of the RFBR 19-38-90278 "Algorithms of Decentralized Coordinated Control for Satellites' Swarms Dynamics".

Approbation of the work

The main results of the work were reported at the following conferences: 5th IAA Conference on University Satellite Missions and CubeSat Workshop (2020), 71st International Astronautical Congress, The CyberSpace Edition (2020).

Publications

The main results on the topic of the dissertation are presented in 4 printed works in peer-reviewed journals included in the international citation systems Web of Science and Scopus.

1. Anton Afanasev, Shamil Biktimirov. CubeSats formation architecture for small space debris surveillance and orbit determination // Informatsionno-upravliaiushchie sistemy [Information and Control Systems], 2021, no. 4, P. 37–46, DOI: 10.31799/1684-8853-2021-4-37-46.

2. Anton Afanasev, Mikhail Shavin, Anton Ivanov, Dmitry Pritykin. Tetrahedral satellite formation: Geomagnetic measurements exchange and interpolation//

Advances in Space Research, 2021, Vol. 67, no. 10, P. 3294–3307, DOI: 10.1016/j.asr.2021.02.012 (Scopus Q2).

3. Anton Afanasev, Anton Ivanov. Attitude control algorithms aided by multipoint statistics and distributed measurements processing in a swarm of cubeSats // Proceedings of the International Astronautical Congress, IAC-20. 2020.

4. Anton Afanasev, Anton Ivanov, Ahmed Mahfouz, Dmitry Pritykin. Attitude control algorithms in a swarm of cubesats: Kriging interpolation and coordinated data exchange // Advances in the Astronautical Sciences, 2020, Vol. 173.

Personal contribution of the author

The main finding of the thesis was obtained either by the applicant in person, or in collaboration with co-authors where the role of the applicant was dominant. The numerical implementations of all the algorithms and other computer programs were fulfilled by the applicant personally.

The Content of the Work

The **Introduction** substantiates the relevance of research conducted within the framework of this dissertation, formulates the goals and objectives of the thesis research. The main provisions submitted for defense are outlined, their scientific novelty and practical significance are substantiated. Data on the approbation of the work and the personal contribution of the applicant are given. State-of-the-art techniques are discussed. Theoretical minimum on reference frames, orbital mechanics, time scales, geomagnetic field models, rigid body mechanics, Lyapunov-based controller on magnetorquers and Extended Kalman filters is discussed, all necessary equations and derivations are given.

Chapter 1 discusses the Kriging interpolation between a formation of 4 CubeSats in a fixed formation on a near-circular orbit to enhance the attitude determination and control, which comprises of magnetometers and magnetorquers.

As a processing part, Extended Kalman filter uses angular velocity and quaternion components as a state-space vector, and specifies them with measurements of a geomagnetic field. Measurements are compared with known IGRF model and discrepancy between current and required position of a CubeSat diminishes under magnetorquer control actions. Mean-squared errors of an attitude determination with following noise parameters are given in a figure 1: static torque $\mathbf{T}_{\text{stat}} = 0$; standard deviation of torque noise $\sigma_{\text{torque}} = 5\,\text{nN} \cdot \text{m}$; magnetometer bias $\mathbf{B}_{\text{bias}} = 0$; standard deviation of measurement noise $\sigma_{\text{meas}} = 1\,\text{nT}$; standard deviation of environmental noise $\sigma_{\text{env}} = 1\,\text{nT}$. The CubeSat is assumed to be in a circular orbit (altitude $h_{\text{orb}} = 750\,\text{km}$; inclination $i = 60°$). The output of the magnetorquers is limited by $m_{\text{max}} = 0.1\,\text{A} \cdot \text{m}^2$. The control loop time settings are $t_{\text{ctrl}} = 5\,\text{s}$ and $t_{\text{meas}} = 1\,\text{s}$.

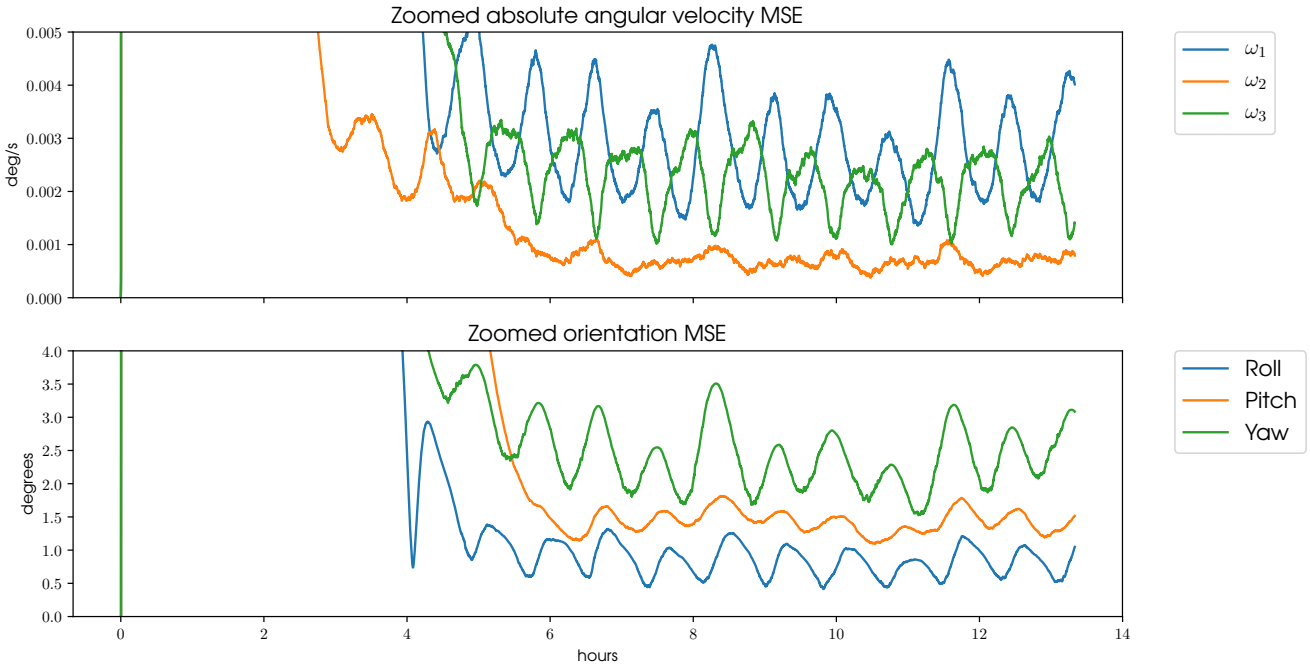

Figure 1: MSE of the absolute angular velocity and Euler angles.

The problem is that magnetometer is a rather noisy sensor and ineffective under

magnetic storm occurrences. To make attitude control more robust and to take advantage of the swarm of spacecraft, we interpolate magnetic field measurements with Kriging technique. Kriging algorithms are a family of linear regression methods to estimate point values at any location within a given region[1],[2].

Unlike inverse distance weighing and splines, which use predetermined analytical formulae defining the smoothness of the resulting curve and dependent only on the measurements of point values in the vicinity of the interpolated location, Kriging is based on the statistical models. The latter include auto correlation analysis (relations between measured points). As a result, Kriging not only constructs predicted values surface, but also provides representation of the reliability or accuracy of such values.

Kriging takes into account spatial correlation between the data points, which is determined by the vector distances between them. The point in the region is denoted by $\mathbf{R}$, and the value of the parameter measured at this point is denoted by $\widetilde{\mathbf{B}}(\mathbf{R})$ (since we measure magnetic field)[3].

The estimator in Kriging is, as in inverse distance weighing, weighted sum of measurements in the vicinity of the interpolated point:

$$\widehat{\mathbf{B}}(\mathbf{R}_0) = \sum_{j=1}^{n} \kappa_j \widetilde{\mathbf{B}}(\mathbf{R}_j), \tag{1}$$

where $\mathbf{R}_0$ – interpolated point, $\widehat{\mathbf{B}}$ – predicted value of the measured parameter, $\mathbf{R}_j$ – available points in the vicinity of interpolated one, κ_j – weights, reflecting the spatial correlation between $\mathbf{R}_j$ and $\mathbf{R}_0$, n – number of available points.

[1] H. Wackernagel, "Multivariate Geostatistics", Berlin, Heidelberg.: Springer, 1995.

[2] T.C. Bailey, A.C. Gatrell, "Interactive Spatial Data Analysis", 1st. Informa PLC, 5 Howick Place, London: Routledge, 1995.

[3] K. Campbell, "Comparing Accuracies of Spatial Interpolation Methods on 1-Minute Ground Magnetometer Readings", MA thesis. North Dakota: North Dakota State University, 2017.

System of equations on weights κ_j and Lagrange multiplier $\varkappa$:

$$\begin{cases} \sum\limits_{j=1}^{n} \kappa_j \gamma(\mathbf{R}_i - \mathbf{R}_j) + \varkappa = \gamma(\mathbf{R}_i - \mathbf{R}_0), \\ \sum\limits_{j=1}^{n} \kappa_j = 1. \end{cases} \tag{2}$$

where $\gamma(\mathbf{R}_i - \mathbf{R}_j)$ is a semivariance:

$$\gamma(\mathbf{R}_i - \mathbf{R}_j) = \frac{1}{2}\mathsf{D}\left[\widetilde{\mathbf{B}}(\mathbf{R}_i) - \widetilde{\mathbf{B}}(\mathbf{R}_j)\right]. \tag{3}$$

To collect the information about the semivariance of the measured parameter in the given region, the empirical semivariogram (ESV) is built. ESV is the non-parametric function, which takes as an argument distance between measured points h and gives as an output approximate semivariance between values points, which are located at a distance h between each other:

$$\begin{aligned} \forall \mathbf{R}_i, \mathbf{R}_j : \quad & |\mathbf{R}_i - \mathbf{R}_j| = h \\ & \gamma(h) = \frac{1}{2n_h} \sum_{(i,j)=1}^{n_h} \left(\widetilde{\mathbf{B}}(\mathbf{R}_i) - \widetilde{\mathbf{B}}(\mathbf{R}_j)\right)^2, \end{aligned} \tag{4}$$

where n_h is the total number of sampled points pairs.

After we have collected enough data in ESV, we can approximate it with some model function, which ensures validity. This is necessary, due to discontinuity of (4). There is a vast majority of such models, but the powered exponential one was the most common out of the best fit:

$$\gamma(h) = \begin{cases} c_0 + c\left(1 - \exp\left\{\left[-\left(\dfrac{h}{a}\right)^{\nu}\right]\right\}\right), & h > 0, \\ 0, & h = 0, \end{cases} \tag{5}$$

On the figure 2 ESV is plotted with power exponential model function. Semivariogram of the direct dipole magnetic field on the circular orbit with altitude $h_{\text{orb}} = 750\,\text{km}$ and inclination $i = 60°$. $n = 2000$ points are taken in the vicinity of the point on orbit with argument of latitude $u = 60°$ ($n_h = 19900$ averaged to

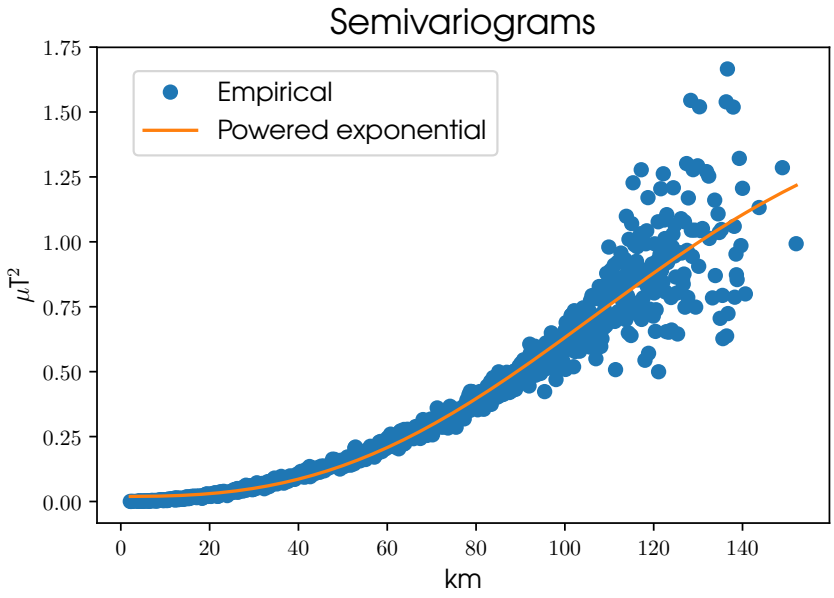

Figure 2: Semivariogram of the direct dipole.

1000). The vicinity is defined as the cube with center in the point of the orbit and sides, equal to 50 km.

As the result, the semivariogram with parameters from (5):

- $c_0 = 0.02\,\mu\mathrm{T}^2$,
- $c = 1.5\,\mu\mathrm{T}^2$,
- $a = 127\,\mathrm{km}$,
- $\nu = \dfrac{8}{3}$,

will be used for swarm scenario filtering.

Simulation results of filtering with Kriging are presented in the figure 3. Plots are given only for 1 satellite out of 4, because the results a similar. Parameters of the orbit, CubeSats, controller and noises are the same as in the single satellite scenario. In comparison with the figure 1 the accuracy of the orientation in the current plot is one degree better, which is the best case in simulations. It shows that the Ordinary Kriging interpolation does ensure an attitude control enhancement.

In previous chapter interpolation for swarm with fixed distances was discussed. In reality, such motion of a group of satellites is possible with specific thrust impulses,

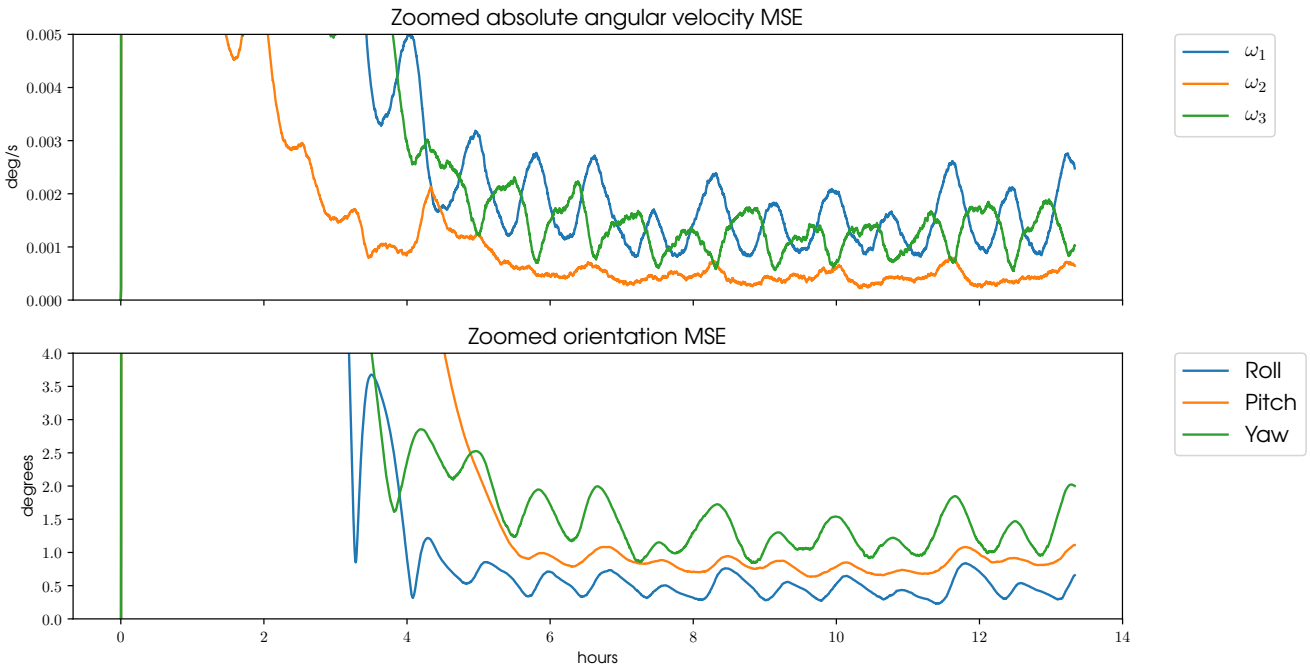

Figure 3: MSE of the absolute angular velocity and Euler angles in swarm scenario.

which usually are very costly. That's why in **Chapter 2** we propose a formation that is not only used to collect the measurement data, but can also provide a real-time service to a larger swarm mission, whose satellites may be distributed over the interior of the servicing formation. As an example of such service the interpolation of geomagnetic field in the interior points of the four-satellite tetrahedral formation is considered, which will be feasible for ionospheric missions. We consider an example of ionospheric mission (such as to study ionospheric polar plasma irregularities), so the formation will be deployed at a near polar circular orbit with altitude of 500 km and inclination of 87°. We shall assume that a certain reference point is traveling along this orbit, whereas the four satellites occupy specially constructed near circular relative orbits such that the four spacecraft positions are in the vertices of a non-degenerate tetrahedron.

Relative motion of two closely orbiting satellites in the central gravity field in near circular orbits is described by the Hill-Clohessy-Wiltshire equations, which are extensively used in formation flying studies[4],[5]. This implies consideration of

[4] G. Hill, "Researches in the lunar theory", American journal of Mathematics 1.1, pp. 5–26, 1878.

[5] R.S. Wiltshire, W.H. Clohessy, "Terminal guidance system for satellite rendezvous", Journal of the

the relative spacecraft dynamics with respect to the orbital reference, whose origin moves along the circular orbit of radius r_0 and the mean motion ω_0.

The linearized equations describing spacecraft relative motion in near circular orbits are given by

$$\begin{cases} \ddot{x} + 2\omega_0 \dot{z} = u_x, \\ \ddot{y} + \omega_0^2 y = u_y, \\ \ddot{z} - 2\omega_0 \dot{x} - 3\omega_0^2 z = u_z, \end{cases} \tag{6}$$

where $\mathbf{u} = \begin{pmatrix} u_x & u_y & u_z \end{pmatrix}^\top = \dfrac{\Delta \mathbf{f}}{m}$, m is the mass of the spacecraft, and $\Delta \mathbf{f}$ is the linearized resultant force acting on the spacecraft, which can include a control force or any disturbing forces. In the case of free motion, i.e. if $\Delta \mathbf{f} = \mathbf{0}_{3\times 1}$, equations (6) admit bounded periodic solutions given by

$$\begin{cases} x(t) = c_1 \cos(\omega_0 t + \alpha_0) + c_3, \\ y(t) = c_2 \sin(\omega_0 t + \beta_0), \\ z(t) = \dfrac{c_1}{2} \sin(\omega_0 t + \alpha_0), \end{cases} \tag{7}$$

where the constants $c_1, c_2, c_3, \alpha_0, \beta_0$ are determined by the initial conditions.

Tetrahedron Formation Initial Conditions					
Satellite	c_1	c_2	c_3	α_0	β_0
Satellite 1	0	0	0	0	0
Satellite 2	$2\rho/5$	0	$2\rho\sqrt{5/3}$	0	0
Satellite 3	2ρ	$\rho\sqrt{5}$	$\rho\sqrt{5/3}$	$-\arctan(1/\sqrt{2})$	$\arctan(\sqrt{2}) - \pi$
Satellite 4	2ρ	$\rho\sqrt{5}$	$\rho\sqrt{5/3}$	$\arctan(1/\sqrt{2})$	$-\arctan(\sqrt{2})$

Table 1: Initial conditions for the tetrahedron vertices reference trajectories.

The initial conditions determining the reference trajectories are specified in Table 1. The value of parameter ρ, which determines the characteristic distances

Aerospace Sciences 27.9, pp. 653–658, 1960.

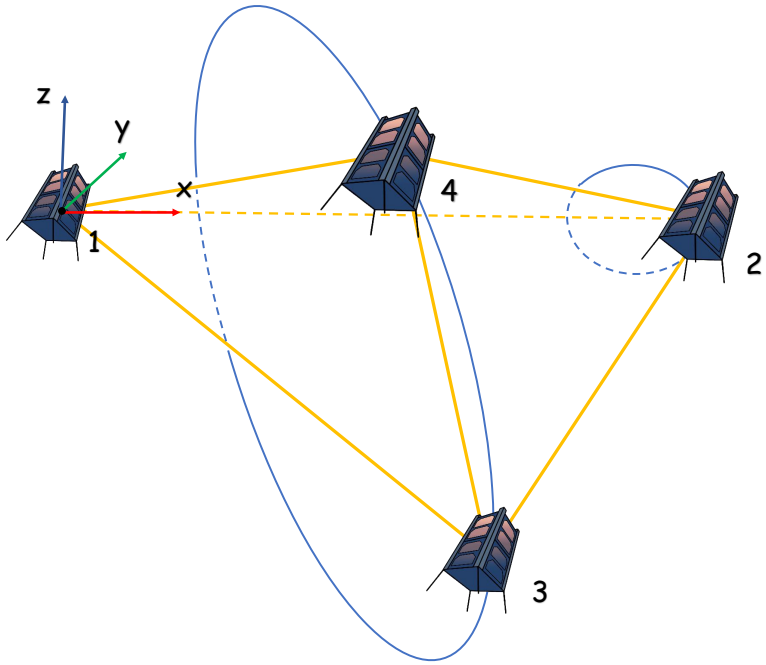

Figure 4: Relative trajectories of the formation satellites as seen from the orbital frame.

between the satellites in formation is chosen to be $\rho = 1430$ m for all subsequent simulations. The relative trajectories and the varying distances between the satellites in the formation are shown in Fig. 4 and Fig. 5a.

The measure of the resulting tetrahedron quality is introduced as:

$$\mathscr{Q} = 12\frac{(3V)^{2/3}}{L}, \tag{8}$$

where V is the volume of the tetrahedron and L is the sum of squared lengths of all tetrahedron's edges[6],[7]. $\mathscr{Q}$ changes between 0 for degenerate configuration and 1 for regular tetrahedrons. Maximizing the minimum quality along the orbit in the central gravity field, one obtains $\mathscr{Q} = 1/\sqrt[3]{5}$[8]. Let us note here that the constants in Table 1 correspond to the initial conditions derived for the maximum quality case.

[6] W. Daly, "The Tetrahedron Quality Factors of CSDS", Max Planck Inst. für Aeronomie Tech. Rep., 1994.

[7] G. Paschmann, W. Daly, "Analysis Methods for Multi-Spacecraft Data", ISSI Scientific Reports Series 1, 1998.

[8] S. Shestakov, M. Ovchinnikov, Ya. Mashtakov, "Analytical Approach to Construction of Tetrahedral Satellite Formation", Journal of Guidance, Control, and Dynamics 42.12, pp. 2600–2614, 2019.

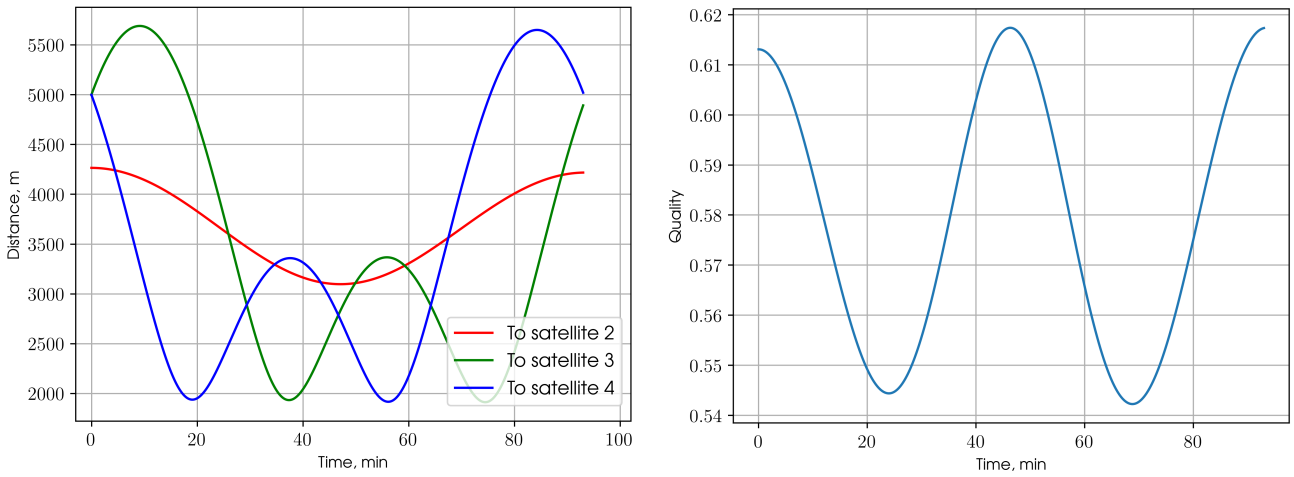

(a) Intersatellite distances

(b) Tetrahedron quality

Figure 5: Distances between the formation satellites and the formation quality.

We can create ESV with the data obtained from IGRF-13 model. It is important to find out how much the interpolation accuracy is influenced by the semivariogram constructed from the IGRF model, if the actual field is different. In other words, the question is how do the IGRF errors influence the resulting empirical semivariogram. In order to quantify the effect, we have analyzed several empirical semivariograms and compared their effect on the Kriging weights. The resulting comparison is presented in Fig. 6.

The baseline semivariogram in this figure is the blue IGRF-13 without any perturbations. Comparing other models with the baseline allows us to draw the conclusion that depending on the noise level for different IGRF models, only the value of the displacement along the ordinate axis changes. The trend is approximately the same.

Taking into account the fact that semvariograms are used as weights of linear system of Eqs. (2), the displacement along the ordinate axis becomes insignificant for the solution. It means that even if the geomagnetic field data come with a large noise component, the results will still be highly relevant for the Kriging approach.

Using powered exponential model function from (5), we approximate ESV from fig. 6. Figures 7 (a), (b) and (c) present the results of fitting powered exponential

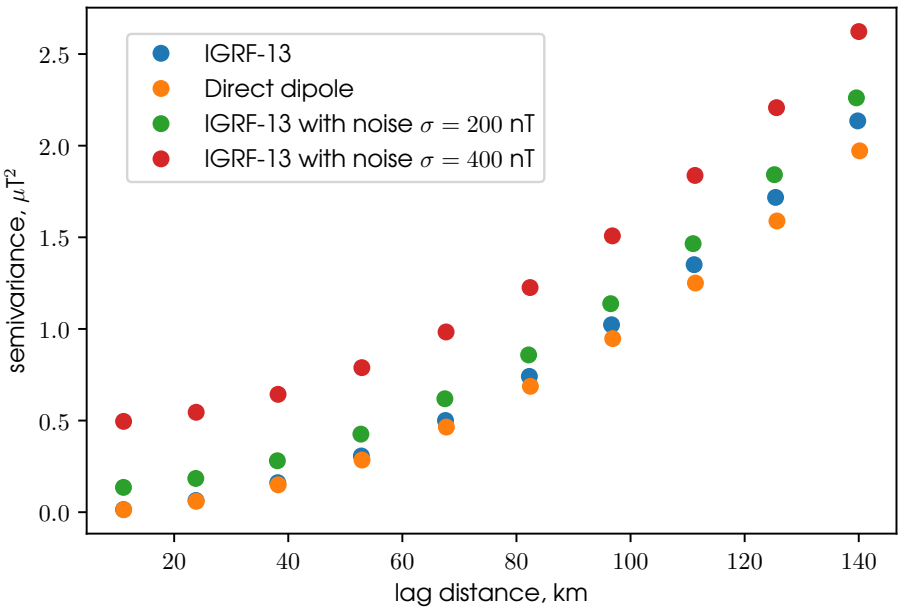

Figure 6: Comparison of ESV trends for different field models.

model to the empirical semivariograms, which are based on the IGRF-13 model without any noise, with 200 nT noise, and with 400 nT noise, respectively. The parameters from Eq. (5) are presented in Table 2.

Standard deviation of model noise, [nT]	c_0, $[\mu T^2]$	c, $[\mu T^2]$	a, [km]	ν
0	0.04	2.48	364	2.77
200	0.15	2.86	390	2.52
400	0.5	2.13	335	2.73

Table 2: Function parameters for different magnetic field models.

As can be seen from Table 2, all parameters except c_0 are nearly the same, which corroborates the assumption about the ordinate displacements for these semivariograms. The assumption of solution robustness in the presence of the noise component in empirical semivariogram is corroborated by multiple numerical experiments.

The graphs of Fig. 8 present the comparison of the geomagnetic field interpolated measurements with a single satellite measurements data. The interpolation is made for the location of satellite 1 along its orbit. The plot depicts the errors

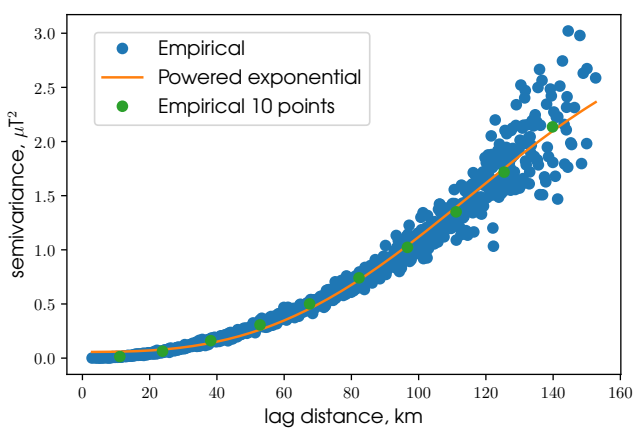

(a) No noise

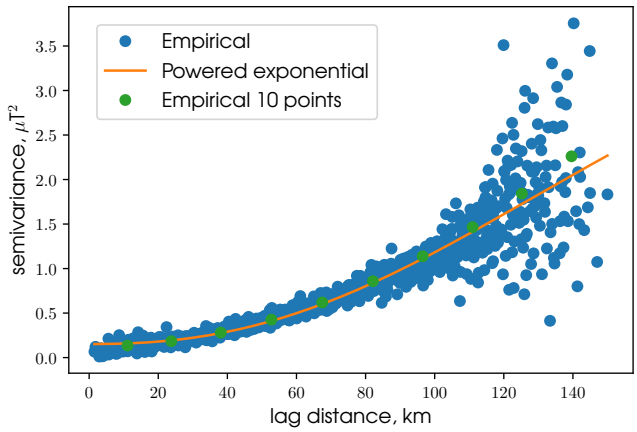

(b) Noise with $\sigma = 200$ nT

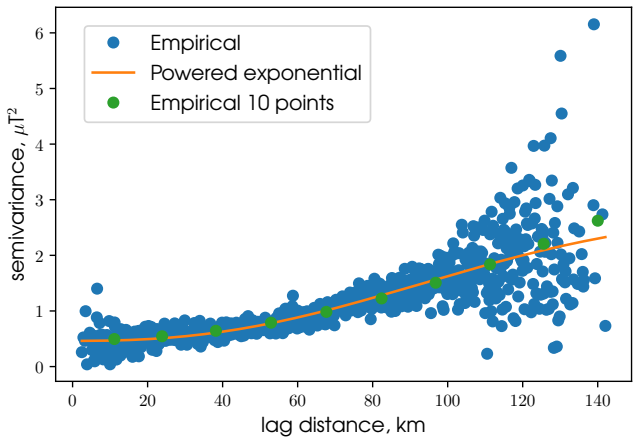

(c) Noise with $\sigma = 400$ nT

Figure 7: Fitting of the powered exponential ESV, based on IGRF-13 models with different level of noise.

of direct measurement of the geomagnetic field (black dots) and the errors of the interpolation results (colored dots). The plots are made for just one run (one orbit) and for the location of just one satellite, however the errors are qualitatively representative of what we obtained in multiple numeric experiments.

Fig. 9, shows how average MSE (for the interpolated absolute value of the geomagnetic field at the locations of all the four satellites along their orbits) is dependant on the characteristic size of this formation. The average is computed from 100 runs of one orbital period and different noise seeds. The dotted horizontal line in the figure is the MSE δ for measurements carried out by each satellite in

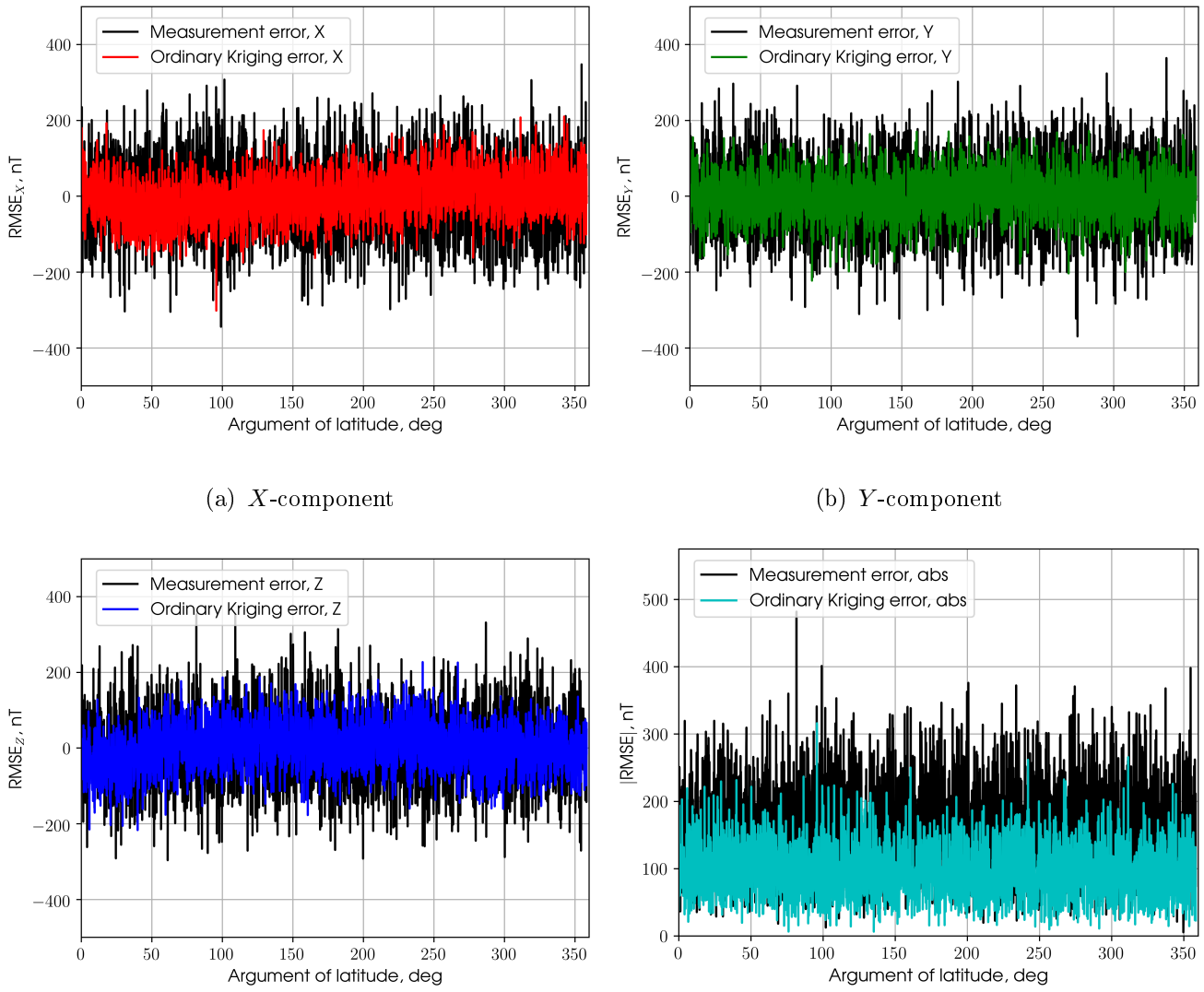

(a) X-component

(b) Y-component

(c) Z-component

(d) Absolute value

Figure 8: MSE of magnetic field interpolation by OK in comparison with measurements MSE of Satellite #1.

singleton mode without interpolation.

To increase the number of points in the vicinity of interpolation, we used measurements history. The usage of measurements history implies adding prior measurements carried out by the formation spacecraft for the current interpolation. The prior measurements are made in the previous locations of the spacecraft along their respective orbits and we have to assume that the measured field does not change during the time that passed since the measurements were made. This limit the history of measurements to those made no earlier than 0.2 seconds prior to the

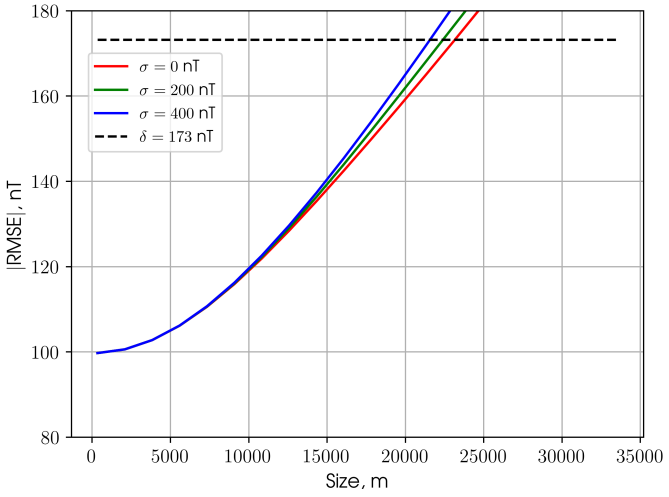

Figure 9: MSE of the magnetic field interpolation versus characteristic size of the formation.

current time, which corresponds to the distance of approximately 1.5 km back along the orbit. Table 3 presents the quantitative comparison of the history experiment results.

Interpolation type	μ_{abs}, [nT]	σ_{abs}, [nT]	σ_X, [nT]	σ_Y, [nT]	σ_Z, [nT]
with history	84.4	91.6	53.2	51.2	54.1
without history	95.9	104.3	60.9	57.7	62.1

Table 3: Comparison of means and estimated standard deviations of the MSEs.

Let's see the effect of magnetic field measurements interpolation on attitude determination and control with TRIAD algorithm. Since it uses a pair of vectors, we add a Sun direction, which can acquired via Sun sensors. Model error is taken as $\sigma_{\text{model}} = 500$ nT and $\sigma_{\text{sun model}} = 10^{-9}$, measurements errors are $\sigma_{\text{mm}} = 10$ nT and $\sigma_{\text{sun sensor}} = 10^{-4}$.

MSE calculation is shown on the fig. 10. Subfigures (a)-(d) show the MSEs of Euler angles, reconstructed with TRIAD algorithms, based on the model values (blue) and interpolated values (orange) of the Earth magnetic field. Subfigures (e)-(f) show the example of Euler angles evolution on the orbit for Satellite #1 and how they are reconstructed with TRIAD, based on interpolated magnetic field

values. Results indicate that the interpolation of geomagnetic field enhances the accuracy of the satellite attitude determination even with simple TRIAD up to 3° in the case of strong divergence of the on-board model with the actual magnetic field.

In **Chapter 3** we consider a number of formation-flying architectures of CubeSats to perform space-based optical observations for on-request orbit determination of smaller (1 to 10 cm in size) space debris objects in SSO. We assume that the formations are deployed into a circular sun-synchronous orbit at 700 km altitude and each spacecraft carries an optical payload to track the debris objects. We discuss the observation conditions and select an orbit close to the terminator plane. We then analyze a construction of an extended information filter to process the multipoint measurements obtained by the formation spacecraft and analyze its OD-accuracy taking into account the payload constraints and depending on such systems parameters as the formation type, number of spacecraft in a formation, and intersatellite distances.

We consider 3 common satellite formation configuration types such as train, GCO and tetrahedron formation. For trade-off analysis we will also test each orbital configuration with different triangulation bases. In order to design the formations' orbital configurations, we employ the Hill-Clohessy-Wiltshire equations from (6) and their bounded solutions (7) with initial condition constants $c_1, c_2, c_3, \alpha_0, \beta_0$.

The orbital configurations used in the study are defined in Table 4, the 3$^{\text{rd}}$ part of which coincides with that of table 1. Parameter ρ defines a triangulation base. In the numerical simulation we use three different values for $\rho = 1, 5, 10$ km. Figures 11-13 depict resulting orbital configurations.

We now consider the simulations for all configurations of the satellites with optical sensors with following parameters: measurement period $T = 1\,\text{s}$, cone angle FWHM = 10°, measurement error $\sigma_{\text{meas}} = 5''$, maximal detectable magnitude $\mathscr{M}_{\max} = 18$.

An average detectable target debris is given following parameters: albedo $\xi =$

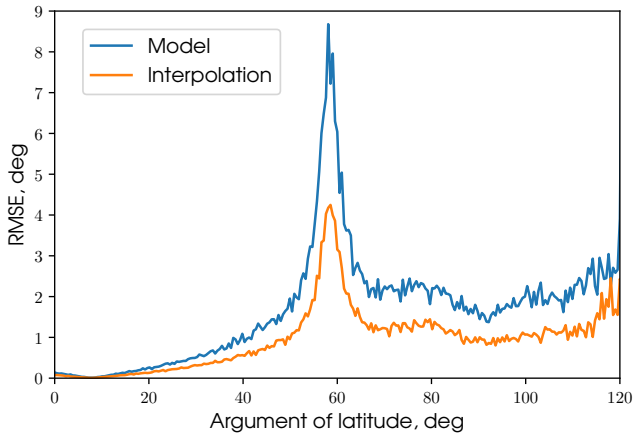

(a) MSE of roll angle

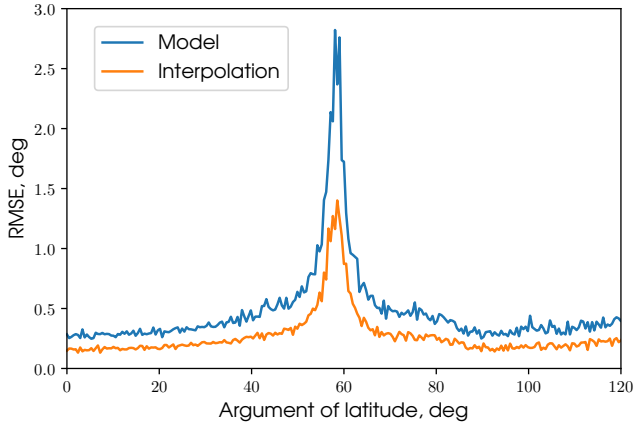

(b) MSE of pitch angle

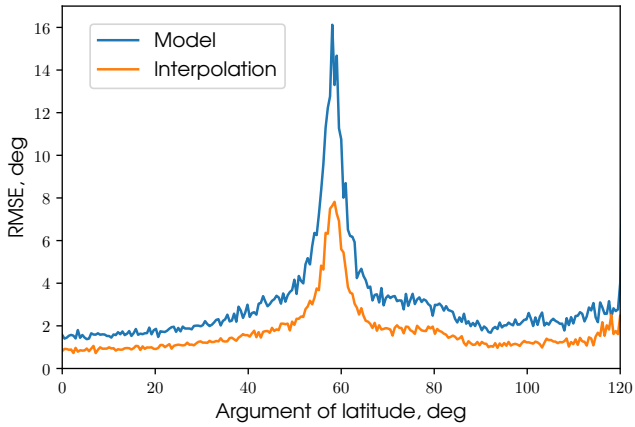

(c) MSE of yaw angle

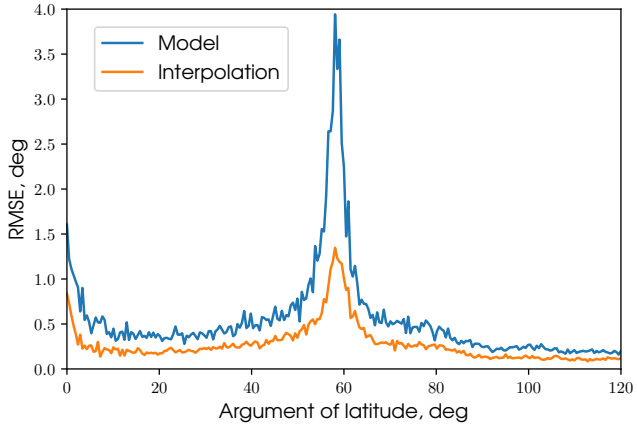

(d) MSE of finite rotation angle

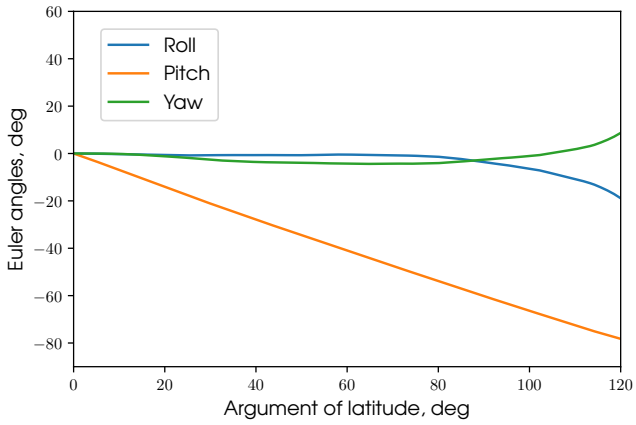

(e) True Euler angles

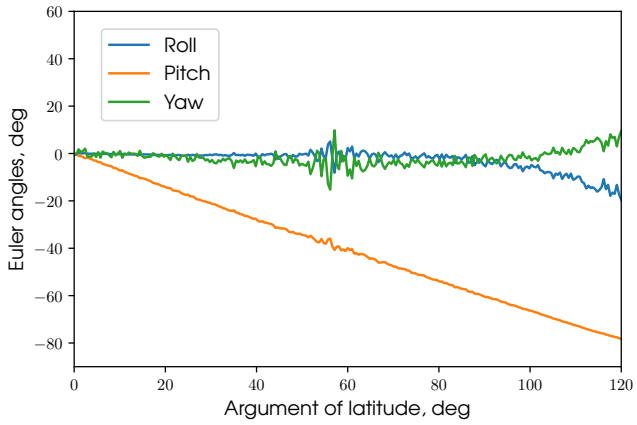

(f) TRIAD-reconstructed Euler angles

Figure 10: The error of Euler angles and quaternion angle determination of Satellite #1, using the TRIAD algorithm.

Satellite #	c_1	c_2	c_3	α_0	β_0
Train formation					
1	0	0	0	0	0
2	0	0	ρ	0	0
3	0	0	$-\rho$	0	0
GCO formation					
1	0	0	0	0	0
2	ρ	$\sqrt{3}\rho/2$	0	0	0
3	ρ	$\sqrt{3}\rho/2$	0	π	π
Tetrahedron formation					
1	0	0	0	0	0
2	$2\rho/5$	0	$2\rho\sqrt{5/3}$	0	0
3	2ρ	$\rho\sqrt{5}$	$\rho\sqrt{5/3}$	$-\arctan\left(1/\sqrt{2}\right)$	$\arctan\left(\sqrt{2}\right)-\pi$
4	2ρ	$\rho\sqrt{5}$	$\rho\sqrt{5/3}$	$\arctan\left(1/\sqrt{2}\right)$	$-\arctan\left(\sqrt{2}\right)$

Table 4: Initial conditions for formations' relative orbits.

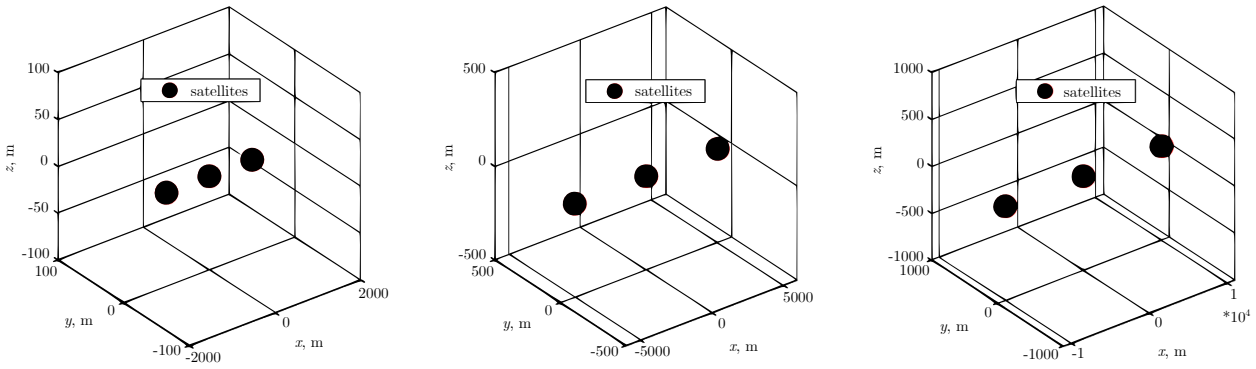

Figure 11: Train formation with base of 1, 5 and 10 km.

0.3, cross-section $A = 0.01\,\mathrm{m}^2$, acceleration error $\sigma_{\mathbf{a}} = 10^{-3}\,\mathrm{m}\cdot\mathrm{s}^{-2}$. The orbit is chosen as the common debris-polluted LEO with parameters: SMA $a_{\mathrm{targ}} = 7177\,\mathrm{km}$, eccentricity $e_{\mathrm{targ}} = 10^{-6}$, inclination $i_{\mathrm{targ}} = 85.4°$, RAAN $\Omega_{\mathrm{targ}} = 136.6°$, AOP $\omega_{\mathrm{targ}} = 0$, TA $\nu_{\mathrm{targ}} = 300°$

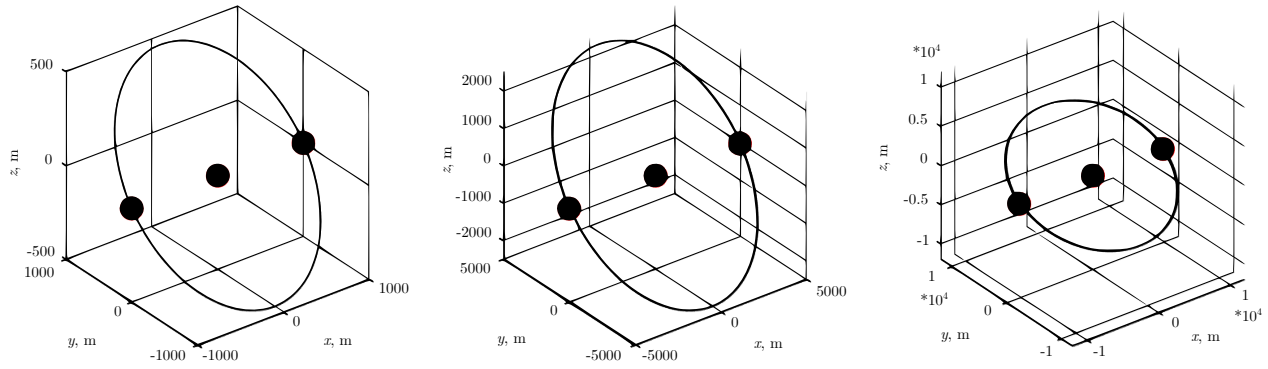

Figure 12: GCO formation with base of 1, 5 and 10 km.

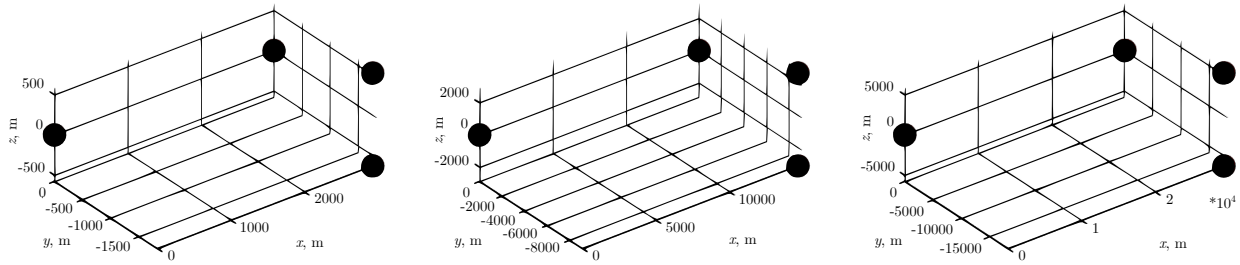

Figure 13: Tetrahedron formation with base of 1, 5 and 10 km.

Simulations are held for $N = 18000$ time steps, with initial state covariance matrix for EIF $\mathbf{P}_0 = \mathrm{diag}\left(\sigma_{r_0}^2 \quad \sigma_{r_0}^2 \quad \sigma_{r_0}^2 \quad \sigma_{v_0}^2 \quad \sigma_{v_0}^2 \quad \sigma_{v_0}^2\right)$, where $\sigma_{r_0} = 10\,\mathrm{km}$ and $\sigma_{v_0} = 10\,\mathrm{m}\cdot\mathrm{s}^{-1}$. Initial state of the state-space vector $\mathbf{X}_0$ coincides with the true value of this vector (that's why the initial error on the graphs will be 0). Simulations are repeated $M = 200$ times to calculate the MSE of the estimated position of the target debris.

The result of all simulations can be seen in tables 5-7. MSEs are taken for each projection of the radius-vector of the target. It's clear, that's the biggest error is located in the Z-coordinate of the target position in all cases. Thus, we are putting it in the tables as the most appropriate one to show the effectiveness of the filter.

The example of MSE simulations is given on figures 14-16. All figures represent GCO configurations for $\rho = 1\,\mathrm{km}$. Figures are related to 2-sensor structure, as an example for synopsis.

Configuration	Number of satellites	MSE [m]			
		$t = 50\,\mathrm{s}$	$t = 100\,\mathrm{s}$	$t = 200\,\mathrm{s}$	$t = 300\,\mathrm{s}$
Train	2	1200	1050	280	200
	3	1070	730	220	190
GCO	2	1150	1000	380	200
	3	1100	700	220	160
Tetrahedron	4	820	660	210	200

Table 5: MSE of the target debris position for sensor configurations with $\rho = 1\,\mathrm{km}$.

Configuration	Number of satellites	MSE [m]			
		$t = 50\,\mathrm{s}$	$t = 100\,\mathrm{s}$	$t = 200\,\mathrm{s}$	$t = 300\,\mathrm{s}$
Train	2	1300	970	300	180
	3	1080	900	300	170
GCO	2	1200	920	230	210
	3	900	550	220	170
Tetrahedron	4	800	790	230	170

Table 6: MSE of the target debris position for sensor configurations with $\rho = 5\,\mathrm{km}$.

Configuration	Number of satellites	MSE [m]			
		$t = 50\,\mathrm{s}$	$t = 100\,\mathrm{s}$	$t = 200\,\mathrm{s}$	$t = 300\,\mathrm{s}$
Train	2	1250	1050	360	200
	3	1110	820	300	190
GCO	2	1310	1100	260	180
	3	980	680	260	170
Tetrahedron	4	990	720	340	220

Table 7: MSE of the target debris position for sensor configurations with $\rho = 10\,\mathrm{km}$.

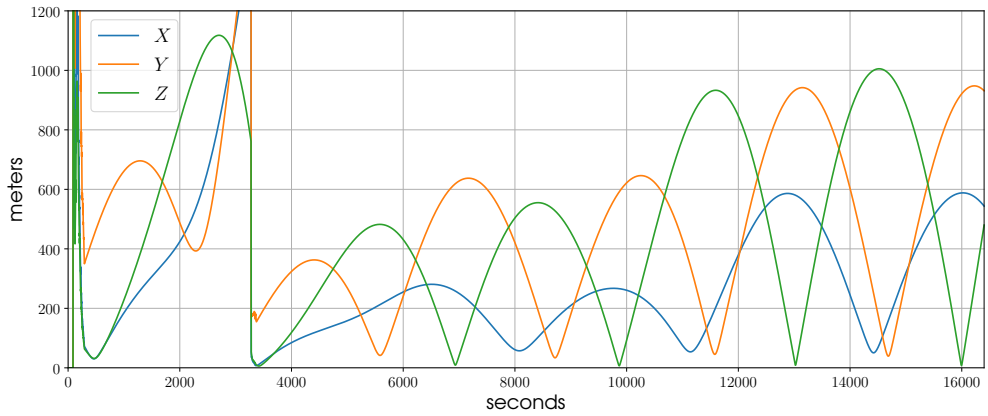

Figure 14: MSE of the target debris position determination from 2 optical sensors within satellites in GCO configuration with $\rho = 1\,\text{km}$ and measurement time of $t = 100\,\text{s}$.

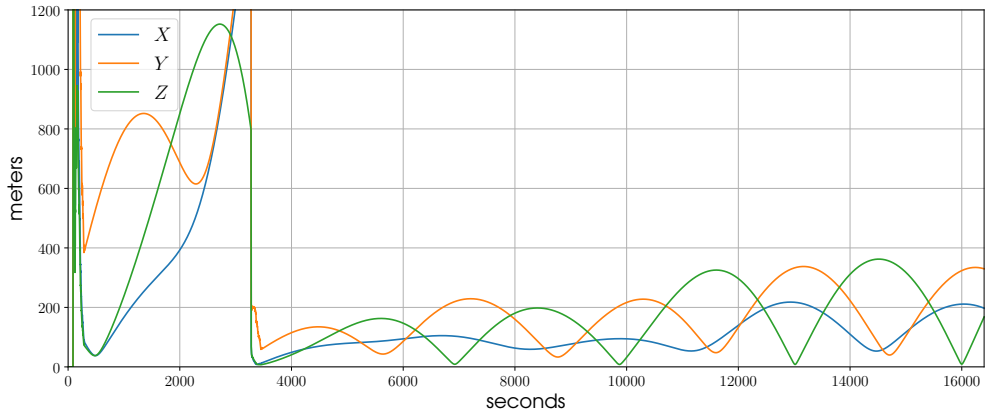

Figure 15: MSE of the target debris position determination from 2 optical sensors within satellites in GCO configuration with $\rho = 1\,\text{km}$ and measurement time of $t = 200\,\text{s}$.

An amount of satellites also decreases the error of position estimation. So, for 2 satellites in small times of measurement MSEs are actually worst. The situation flattens out as the time of observation increases – for times of 300 s errors for all different number of satellites are basically same, near 180 m.

The type configuration seems to have rather low impact on the MSE of the target position determination, but the results of simulations imply that GCO type of formation gives better results than the train type. Tetrahedral sensor composition is actually incomparable with that of GCO and train because of the different amount

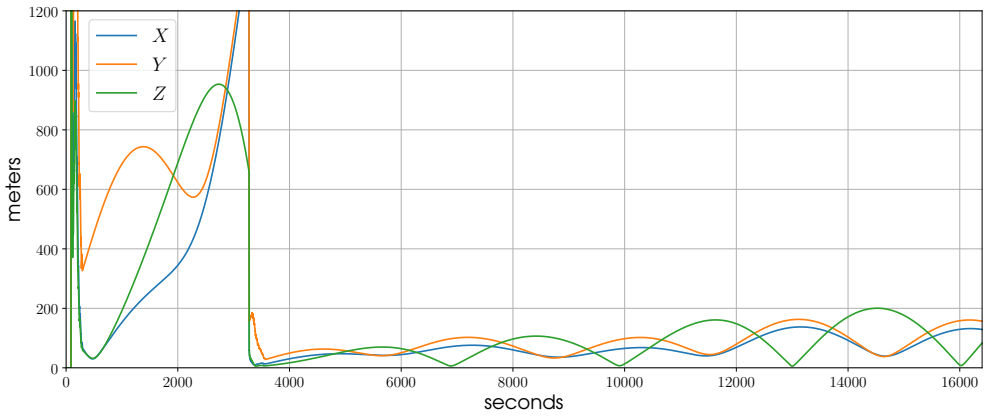

Figure 16: MSE of the target debris position determination from 2 optical sensors within satellites in GCO configuration with $\rho = 1\,\mathrm{km}$ and measurement time of $t = 300\,\mathrm{s}$.

of satellites in those groups, but since this configuration is direct extension of GCO on the 4-point measurement system, we can claim that the tetrahedral formation is the best fit for our purposes. Thus, we recommend to use tetrahedral configuration in the problem of short-arc tracking of target debris.